The Role of Ocean Heat Transport in the Global Climate Response to Projected Arctic Sea Ice Loss

ROBERT A. TOMAS AND CLARA DESER

Climate and Global Dynamics Division, National Center for Atmospheric Research,[a] Boulder, Colorado

LANTAO SUN

Cooperative Institute for Research in Environmental Sciences, University of Colorado Boulder, and NOAA/Earth System Research Laboratory, Boulder, Colorado

ABSTRACT

The purpose of this study is to elucidate the individual and combined roles of thermodynamic and dynamic ocean–atmosphere coupling in the equilibrium global climate response to projected Arctic sea ice loss using a suite of experiments conducted with Community Climate System Model, version 4, at 1° latitude–longitude spatial resolution. The results highlight the contrasting spatial structures and partially compensating effects of thermodynamic and dynamic coupling. In combination, thermodynamic and dynamic coupling produce a response pattern that is largely symmetric about the equator, whereas thermodynamic coupling alone yields an antisymmetric response. The latter is characterized by an interhemispheric sea surface temperature (SST) gradient, with maximum warming at high northern latitudes decreasing toward the equator, which displaces the intertropical convergence zone (ITCZ) and Hadley circulation northward. In contrast, the fully coupled response shows enhanced warming at high latitudes of both hemispheres and along the equator; the equatorial warming is driven by anomalous ocean heat transport convergence and is accompanied by a narrow equatorward intensification of the northern and southern branches of the ITCZ. In both cases, the tropical precipitation response to Arctic sea ice loss feeds back onto the atmospheric circulation at midlatitudes via Rossby wave dynamics, highlighting the global interconnectivity of the coupled climate system. This study demonstrates the importance of ocean dynamics in mediating the equilibrium global climate response to Arctic sea ice loss.

1. Introduction

One of the most visible consequences of human-induced climate change is the melting of sea ice in the Arctic. Climate models project an almost complete loss of perennial Arctic sea ice cover by the end of this century or sooner if current rates of greenhouse gas emissions continue. The disappearance of sea ice will profoundly alter the surface energy balance of the Arctic Ocean as the highly reflective ice cover is replaced by darker open water (e.g., Serreze and Barry 2011). Without the insulating effect of sea ice, the newly exposed warm surface waters will flux heat and water vapor into the overlying atmosphere, warming and moistening the lower troposphere (e.g., Screen and Simmonds 2010). Winds will mix the excess heat and moisture southward over the adjacent continents, increasing temperature and precipitation at high latitudes (Deser et al. 2010). Northern land areas are also expected to experience a decrease in surface temperature variance (Screen et al. 2015a; Sun et al. 2015) and an increase in warm extremes (Screen et al. 2015b) as a result of Arctic sea ice loss.

In addition to local thermodynamic effects, diminished Arctic sea ice cover will weaken the tropospheric westerly winds along the poleward flank of the jet stream in association with a reduced north–south temperature gradient due to enhanced lower-tropospheric warming in the Arctic (Deser et al. 2010; Peings and Magnusdottir 2014; Deser et al. 2015, hereafter D15; Harvey et al. 2014, 2015; Sun et al. 2015). Influences on the

---

north–south meandering of the jet stream and associated synoptic activity including blocking events are less certain (Barnes 2013; Screen and Simmonds 2013; Cohen et al. 2014; Barnes and Screen 2015). In some regions (e.g., central Eurasia) Arctic sea ice loss may paradoxically lead to surface cooling as a result of an enhanced Siberian anticyclone (Mori et al. 2014; Sun et al. 2015), which advects colder air from the northeast, outweighing the thermodynamically induced warming from Arctic sea ice loss.

While most of the climate impacts from Arctic sea ice loss are expected to occur at middle and high latitudes, recent work has shown that ocean–atmosphere coupling may extend the reach of these impacts into the tropics and Southern Hemisphere (D15). The dynamical ocean response, in particular, plays a key role in communicating the effects of Arctic sea ice loss to the entire globe via a weakening of the northward oceanic heat transport. The resulting dynamically induced warming of the tropical oceans intensifies the intertropical convergence zones (ITCZs) on their equatorward flanks, which in turn alters the midlatitude atmospheric circulation via Rossby wave dynamics. In contrast, the thermodynamic air–sea coupled response to Arctic sea ice loss produces a very different tropical response, shifting the Hadley circulation toward the Northern Hemisphere (NH). A similar thermodynamic coupled response to an extratropical thermal perturbation has been found in many idealized modeling studies (Chiang and Bitz 2005; Kang et al. 2008; Frierson and Hwang 2012; Chiang and Friedman 2012; Cvijanovic and Chiang 2013; Seo et al. 2014; Schneider et al. 2014). Although the fundamental role of ocean dynamics in the global coupled response to Arctic sea ice loss was implicated in D15, they did not investigate the global patterns and mechanisms of this response in detail.

The purpose of this study is to explicitly elucidate the role of ocean dynamics in the equilibrium climate response to Arctic sea ice loss beyond that in D15 using a new series of experiments conducted with a slab-ocean coupled model in which changes in sea ice and ocean dynamics are prescribed separately and in combination. The results of these experiments reveal that thermodynamic and dynamic ocean feedbacks have contrasting and largely compensating effects on the remote equilibrium climate response to Arctic sea ice loss. Although our study focuses on the specific problem of Arctic sea ice loss, the results may generalize to other types of climate perturbations.

The rest of this paper is organized as follows. The models, experimental strategy, and design are provided in section 2. Results are presented in section 3.

Key findings are discussed in section 4. Conclusions are given in section 5.

2. Models and experimental design

a. Overview of modeling strategy

Our objective is to separate the roles of dynamic versus thermodynamic ocean feedbacks in the equilibrium coupled climate response to projected late twenty-first-century Arctic sea ice loss within a consistent modeling framework. To accomplish this goal, we use a two-step approach. First, we make use of the coupled model simulations presented in D15, each of which is forced with the same twenty-first-century Arctic sea ice loss but employs a different ocean model configuration (thermodynamic slab or full-depth dynamic ocean). The slab-ocean coupled model experiment isolates the thermodynamic component of the ocean's response to Arctic sea ice loss, while the full-depth ocean coupled model experiment yields the sum of the thermodynamic and dynamic responses. In our second step, we diagnose the ocean heat transport response to Arctic sea ice loss from the full-depth ocean coupled model experiment. We then specify this change in ocean heat transport, in conjunction with twenty-first-century Arctic sea ice loss, to the slab-ocean coupled model. The similarity of the climate responses in this new slab-ocean experiment and the original full-depth ocean model experiment from D15 allows us to isolate the role of ocean dynamics using a consistent framework of the slab-ocean coupled model. Specifically, we obtain the role of ocean dynamics by subtracting the slab-ocean experiment forced with sea ice loss alone from the one forced with ice loss plus ocean heat transport change. Details of the model configurations, experimental design, and late twenty-first-century Arctic sea ice loss are given below. Additional information may be found in D15.

b. Model configurations

The results in this study are based on simulations with the Community Climate System Model, version 4 (CCSM4; Gent et al. 2011), a coupled ocean–atmosphere–land–cryosphere global climate model, configured to run with different representations of the ocean. These are, in decreasing order of physical completeness, 1) a full-depth dynamical ocean model, the Parallel Ocean Program, version 2 (POP2); 2) a slab (mixed layer) ocean model; and 3) no interactive ocean—SSTs and sea ice are prescribed as a lower boundary condition for the atmosphere. All three use the same atmospheric model, the Community Atmosphere Model version 4 (CAM4) with a finite volume dynamical

TABLE 1. Details of the model experiments. See sections 2c–e for definitions of the model experiment acronyms.

Experiment	CCSM4 configuration	OHT or ICE and SST	Arctic sea ice period	Years of simulation
ICE20_FOM	Coupled: FOM	Prognostic OHT	1980–99	360
ICE21_FOM	Coupled: FOM	Prognostic OHT	2080–99	360
ICE20_SOM_Q20	Coupled: SOM	Prescribed OHT ICE20_FOM	1980–99	300
ICE21_SOM_Q20	Coupled: SOM	Prescribed OHT ICE20_FOM	2080–99	300
ICE21_SOM_Q21	Coupled: SOM	Prescribed OHT ICE21_FOM	2080–99	300
ICE21_AMIPG_Q20	Uncoupled AMIP	Prescribed ICE and SST ICE21_SOM_Q20	2080–99	260
ICE21_AMIPG_Q21	Uncoupled AMIP	Prescribed ICE and SST ICE21_SOM_Q21	2080–99	260
ICE21_AMIPT_Q21	Uncoupled AMIP	Prescribed ICE and SST ICE21_SOM_Q21 15°S–15°N; ICE21_SOM_Q20 elsewhere	2080–99	260

core, at a horizontal resolution of 0.90° latitude and 1.25° longitude and 26 vertical levels coupled to the same land model, the Community Land Model version 4 (CLM4), that shares the atmospheric model's horizontal grid. POP2 has a spatial resolution of 1.14° longitude and variable spacing in latitude (0.28° at the equator increasing to 0.66° at approximately 60°N) and 60 vertical levels (20 in the upper 200 m). The experiments with the full-depth dynamical ocean model (FOM) include the CCSM4 dynamic–thermodynamic sea ice module that incorporates a subgrid-scale ice thickness distribution, energy-conserving thermodynamics, and elastic–viscous–plastic dynamics (Holland et al. 2012).

The experiments using the slab-ocean model (SOM) configuration of CCSM4, here termed CCSM4_SOM, employ a fixed-depth mixed layer ocean model without dynamics in place of the FOM. The CCSM4_SOM uses spatially varying but constant-in-time (annual mean) mixed layer depths (MLDs) derived from the CCSM4 climatology; all other model components (including sea ice) are identical to those in the fully coupled configuration (Bitz et al. 2012). To represent the mean effects of ocean heat transport (OHT) on SST, a climatological monthly Qflux term is specified for the CCSM4_SOM. Details of the Qflux and MLD specification are provided in section 2d.

The final configuration of CCSM4 used in this study is one in which only the atmosphere, land, and thermodynamic sea ice model components are active: SST and sea ice (concentration and thickness) are prescribed as monthly climatologies derived from the CCSM4_SOM simulations. Details of the SST and sea ice forcing for these simulations are provided in section 2e.

c. Coupled full-depth ocean model experiments with constrained sea ice

We make use of the FOM coupled experiments from D15 in which the seasonal cycles of Arctic sea ice concentration and thickness are controlled artificially through a longwave radiative flux (LRF) term applied to the sea ice model only. The LRF formulation is designed to achieve Arctic sea ice conditions representative of the late twentieth century (1980–99) and late twenty-first century (2080–99) as simulated by CCSM4 under historical and representative concentration pathway 8.5 (RCP8.5) radiative forcing, respectively. In both LRF experiments, radiative forcing conditions are held fixed at the year 2000 so that the response to sea ice loss, obtained by differencing the two simulations, can be isolated. These constrained sea ice coupled model experiments are denoted ICE20_FOM and ICE21_FOM for the late twentieth- and late twenty-first-century sea ice states, respectively (Table 1), and correspond to ICE_coupled_20 and ICE_coupled_21 in D15's nomenclature. Each experiment is run for 360 years; results presented here are based on averages over the last 260 years when the simulations have reached a quasi-equilibrium state (see D15). A brief summary of the methodology used to control the sea ice in each experiment is given below; a full description may be found in D15.

In both ICE20_FOM and ICE21_FOM, Arctic sea ice concentration and thickness are controlled by specifying an additional LRF to the sea ice model in the Arctic only. We emphasize that 1) the entirety of the prescribed LRF goes directly into the sea ice model component (e.g., the LRF is a "ghost flux" to both the atmosphere and ocean model components), 2) there is no conduction of heat between the sea ice and ocean model components, and 3) the amount of LRF specified to the ice model at a particular grid box at any given time is proportional to the ice fraction in the grid box at that time. Thus, the prescribed LRF does not directly affect the climate system: it impacts the ocean and atmosphere only via the LRF-induced changes in Arctic sea ice. The LRF values used in both experiments are documented in the appendix of D15. A similar strategy was employed in Sewall and Sloan (2004) except that their method of "flux adjustment" was applied to surface temperature, affecting both the sea ice and ocean model components over the entire Arctic; thus, their experimental design does not isolate the response to sea ice loss alone.

TABLE 2. Details and objectives for deriving the responses from the model experiments. The acronym following the symbol Δ denotes the quantity that changes between the two simulations being differenced. Model experiment acronyms are as in Table 1. See sections 2c–e for details.

Name	Simulations differenced	Objective	Ocean model and/or SSTs
ΔICE_FOM	ICE21_FOM minus ICE20_FOM	Coupled response to projected Arctic sea ice loss: sensitivity to ocean model representation.	FOM
ΔICE_SOM_Q20	ICE21_SOM_Q20 minus ICE20_SOM_Q20		SOM, Qflux from ICE20_FOM
ΔICE_SOM_ΔQ	ICE21_SOM_Q21 minus ICE20_SOM_Q20		SOM, Qflux from ICE21_FOM and ICE20_FOM
ICE21_SOM_ΔQ	ICE21_SOM_Q21 minus ICE21_SOM_Q20	Isolating the response to $-\nabla \cdot \Delta$OHT from ΔICE_FOM: what are the effects of tropical SST changes?	SOM
ICE21_AMIPG_ΔQ	ICE21_AMIPG_Q21 minus ICE21_AMIPG_Q20		Prescribed global SST
ICE21_AMIPT_ΔQ	ICE21_AMIPT_Q21 minus ICE21_AMIPT_Q20		Prescribed tropical SST

Lehner et al. (2013) adopted a similar methodology to the one used here to study the role of sea ice feedbacks in the inception of the Little Ice Age.

The difference between ICE21_FOM and ICE20_FOM, referred to as ΔICE_FOM, isolates the coupled response of CCSM4 to GHG-induced Arctic sea ice loss (Table 2). The statistical significance of all responses is assessed using a two-sided Student's t test.

### d. Coupled slab-ocean model experiments with constrained sea ice

We also make use of a parallel set of constrained sea ice experiments with CCSM4_SOM conducted by D15 that are identical in design to those described above for CCSM4_FOM except for the ocean model configuration. In particular, the same LRF values that were applied in the CCSM4_FOM simulations are specified in the CCSM4_SOM simulations, with resulting Arctic sea ice distributions that are very similar between the two model configurations (Fig. 1b). We shall refer to the constrained sea ice SOM simulations as ICE20_SOM_Q20 and ICE21_SOM_Q20, corresponding to Arctic sea ice conditions in the late twentieth and late twenty-first centuries, respectively (Table 1; note that D15 termed these ICE_som_20 and ICE_som_21). Here, Q20 denotes that the same late twentieth-century Qflux term is prescribed in both experiments. This spatially varying climatological Qflux term represents the mean effects of ocean heat transport on SST and is obtained as the residual of the net heat flux into the ocean upper surface and a fictitious change in heat content in the upper ocean (Bitz et al. 2012) derived from the monthly mean climatologies of SST and net surface heat flux and annual-mean climatology of mixed layer depth in ICE20_FOM. MLDs in ICE20_SOM_Q20 and ICE21_SOM_Q20 are specified as spatially varying annual-mean climatologies

derived from ICE20_FOM. The SOM experiments are run for 300 years with radiative forcings fixed at year-2000 values and initialized in an identical manner as the FOM runs (see D15). Results presented here are based on averages over the last 260 years when the simulations have reached a quasi-equilibrium state. The difference between ICE21_SOM_Q20 and ICE20_SOM_Q20, referred to as ΔICE_SOM_Q20, represents the thermodynamically coupled response to GHG-induced Arctic sea ice loss (Table 2).

For this study, we conducted a new SOM experiment, named ICE21_SOM_Q21, that is similar in design to ICE21_SOM_Q20 except that the late twenty-first-century Qflux (Q21), derived from ICE21_FOM, is used. The difference between ICE21_SOM_Q21 and ICE20_SOM_Q20 (ΔICE_SOM_ΔQ; Table 2) isolates the coupled response to the combined effects of Arctic sea ice loss and the change in ocean heat transport induced by the ice loss. Note that differences in SSTs between ICE21_SOM_Q21 and ICE20_SOM_Q20 are due to both dynamic and thermodynamic processes. As we shall show, the responses in ΔICE_SOM_ΔQ closely resemble those in ΔICE_FOM as expected from the experimental design. This demonstrated similarity validates the use of the difference between ICE21_SOM_Q21 and ICE21_SOM_Q20 (ICE21_SOM_ΔQ; Table 2) to isolate the role of ocean heat transport response to Arctic sea ice loss in the overall climate response to Arctic sea ice loss using the common SOM framework.

e. Atmosphere-only model experiments with prescribed boundary conditions

We also conducted a set of experiments using CCSM4 configured with only the atmosphere and land components active (e.g., CAM4–CLM4): SSTs and sea ice concentration and thickness are specified as a lower

Sea Ice Concentration (%)

a)
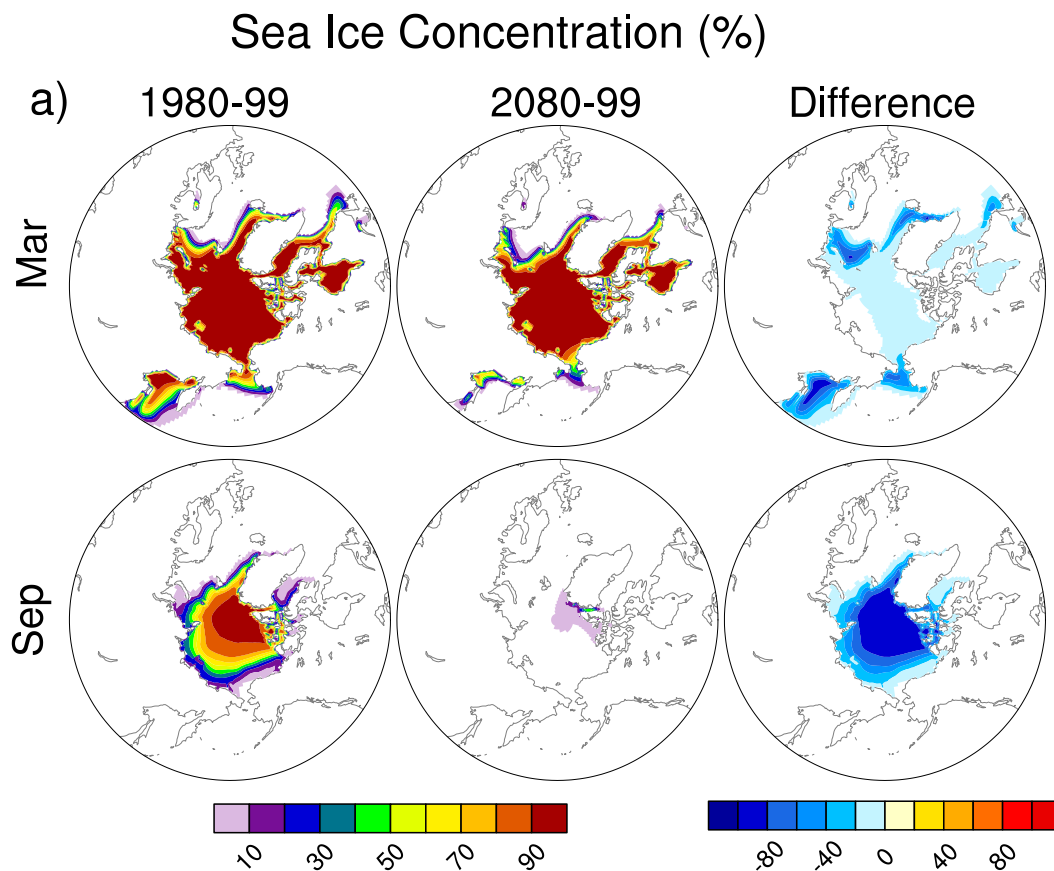
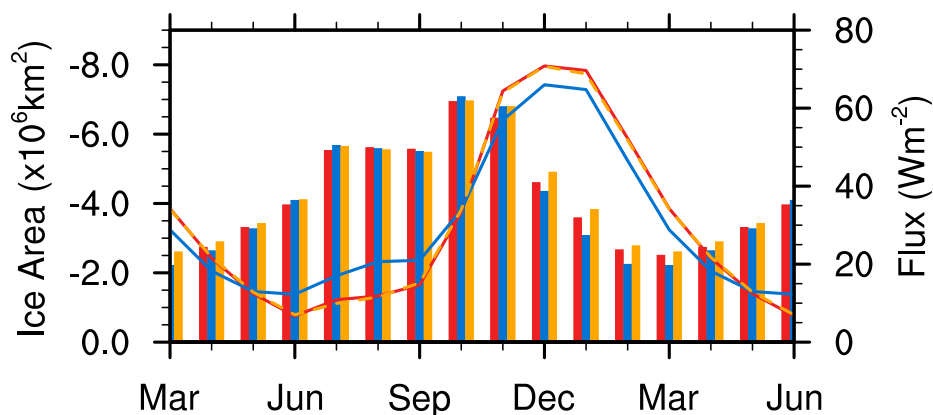b) Ice Area (bars) & Sfc Energy Flux (curves)

FIG. 1. (a) March and September Arctic sea ice concentration (%) in the late (left) twentieth and (center) twenty-first centuries as simulated in ICE20_FOM and ICE21_FOM, respectively, including (right) their difference. (b) Seasonal cycle of area (bars) of Arctic sea ice loss (10^6 km^2) and Arctic net surface heat flux response (curves; W m^{-2}) in ΔICE_FOM (red), ΔICE_SOM_Q20 (blue), and ΔICE_SOM_ΔQ (orange). Note the inverted scale for sea ice area.

boundary condition following the Atmospheric Model Intercomparison Project (AMIP) convention. In these experiments, termed ICE21_AMIPG_Q21 and ICE21_AMIPG_Q20, global distributions of climatological monthly SSTs and sea ice concentration and thickness from ICE21_SOM_Q21 and ICE21_SOM_Q20 are prescribed to CAM4/CLM, respectively. Here, AMIPG indicates that the global domain was used for the SST and sea ice specification (Table 1). The difference between these two AMIP experiments, referred to as ICE21_AMIPG_ΔQ, isolates the effect of the ocean heat transport response to Arctic sea ice loss on the atmosphere through its influence on SST (Table 2). Both AMIP experiments were run for 260 years, and all years were used for analysis.

Close agreement between the atmospheric responses in ICE21_AMIPG_ΔQ and ICE21_SOM_ΔQ (see below) indicates that the AMIP modeling framework can be used as a test bed to further examine the role of regional SST changes. To that end, we conducted an additional 260-yr AMIP experiment, ICE21_AMIPT_Q21, in which only the tropical (15°S–15°N; hence the term AMIPT) portion of the SST field from ICE21_SOM_Q21 is used, with the remainder specified from ICE21_SOM_Q20 (Table 1). The difference between ICE21_AMIPT_Q21 and ICE21_AMIPG_Q20, denoted ICE21_AMIPT_ΔQ, isolates the role of the tropical SST response in ICE21_AMIPG_ΔQ (and correspondingly ICE21_SOM_ΔQ) in driving the atmospheric response to Arctic sea ice loss (Table 2).

f. Projected Arctic sea ice loss and net surface energy flux response

The distributions of Arctic sea ice concentration (SIC) in ICE20_FOM, ICE21_FOM, and ΔICE_FOM are shown in Fig. 1a for March and September, the months of maximum and minimum sea ice extent, respectively. March shows projected losses mainly in the marginal seas (Sea of Okhotsk and Bering Sea in the Pacific, and Labrador, Greenland, and Barents Seas in the Atlantic), whereas September exhibits a nearly complete loss of ice within the central Arctic. Similar patterns of future sea ice loss are found in the ICE_SOM simulations (not shown). In terms of sea ice area, ΔICE_SOM_Q20 slightly underestimates the amount of ice loss compared with ΔICE_FOM, whereas ΔICE_SOM_ΔQ slightly overestimates it (Fig. 1b). However, the magnitudes of the differences are generally less than 15%.

Decreases in Arctic sea ice are associated with large fluxes of heat from the ocean to the atmosphere as the insulating layer of ice is removed from the sea surface. The response of the net surface heat flux (Qnet) to

Arctic sea ice loss in the SOM and FOM experiments is shown in Fig. 1b, where Qnet is defined as the sum of the latent heat, sensible heat, and longwave radiation fluxes averaged over all Arctic Ocean grid boxes containing at least 50% SIC in March during the late twentieth century. The Qnet response (positive values denote upward flux anomalies) shows a marked seasonal cycle in all three experiments (ΔICE_FOM, ΔICE_SOM_Q20, and ΔICE_SOM_ΔQ), with the largest values (60–80 W m^{-2}) from November through February, lagging the peak season of ice loss by approximately 1–2 months, similar to previous studies (Deser et al. 2010, 2015; Sun et al. 2015). This delay is due to the effect of the seasonal cycle of the climatological air–sea temperature difference, which maximizes during the cold season, on the turbulent energy flux response, as discussed in Deser et al. (2010). The Qnet response is nearly identical between ΔICE_FOM and ΔICE_SOM_ΔQ and is slightly larger (smaller) in ΔICE_SOM_Q20 in summer (winter). The small differences in sea ice loss and Qnet response in the FOM and SOM experiments are unlikely to be important for the results shown below.

3. Results

a. Global surface climate response to Arctic sea ice loss

The annual-mean global SST, precipitation, and SLP responses in ΔICE_FOM and ΔICE_SOM_Q20 are compared in Fig. 2. It is immediately evident that the responses differ considerably between the two model configurations. Two key overarching distinctions are apparent: 1) the global SST response exhibits a high degree of equatorial symmetry in ΔICE_FOM, with enhanced warming at high latitudes in both hemispheres and along the equator, in contrast to the hemispherically asymmetric response in ΔICE_SOM_Q20, which shows pronounced warming in the NH and little SST change in the SH and 2) the tropical response is characterized by an SST warming maximum in the equatorial Pacific and an associated equatorward intensification of precipitation within the ITCZs in ΔICE_FOM, in contrast to a strong cross-equatorial gradient in the SST response and accompanying shift of the ITCZ precipitation into the NH in ΔICE_SOM_Q20, as noted also in D15. Other notable differences include SST cooling (warming) on the northern (southern) flank of the Gulf Stream in ΔICE_FOM, a feature that is entirely absent in ΔICE_SOM_Q20. Although both models show the largest warming at high latitudes of the NH, this signal is mainly confined to the
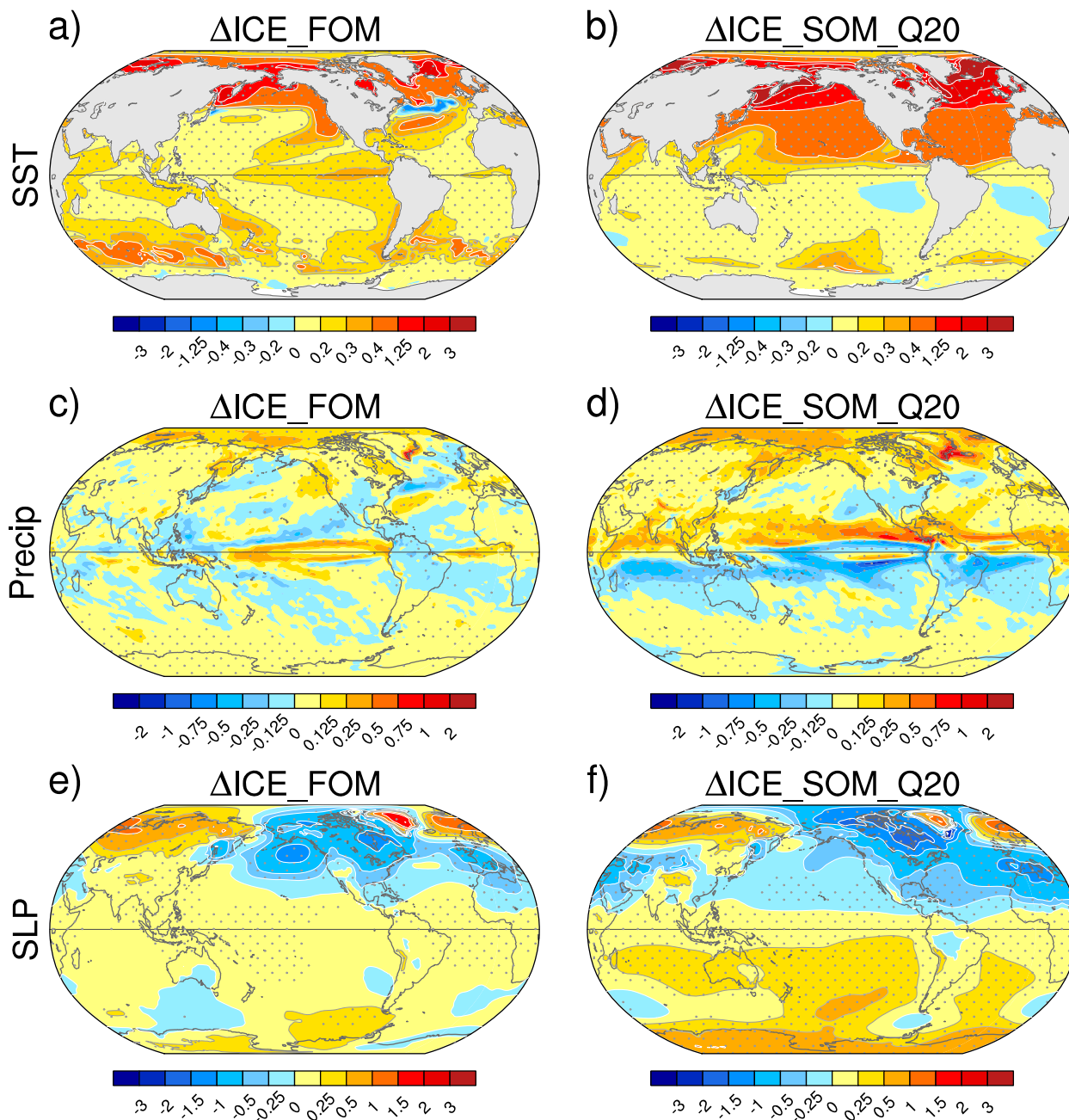
FIG. 2. Annual (a),(b) SST (°C), (c),(d) precipitation (mm day^{-1}), and (e),(f) SLP (hPa) responses to Arctic sea ice loss in (left) ΔICE_FOM and (right) ΔICE_SOM_Q20. Stippling indicates that the response is statistically significant at the 95% confidence level.

extratropics in ΔICE_FOM, whereas it reaches nearly to the equator in ΔICE_SOM_Q20.

The influence of the different SST responses on precipitation is apparent (Figs. 2c,d). The SST anomaly dipole in the vicinity of the Gulf Stream is reflected in a similar precipitation anomaly dipole, with diminished (enhanced) precipitation over the cooler (warmer) SSTs in ΔICE_FOM. In the tropics, the precipitation response in the Pacific sector in

ΔICE_FOM (Fig. 2c) consists of two zonally oriented positive anomaly centers that straddle the equator across much of the basin; both are located slightly equatorward of the climatological precipitation maxima (not shown here but discussed later). The tropical precipitation response is larger in ΔICE_SOM_Q20 than in ΔICE_FOM and is dominated by a strong and overall zonally uniform pattern with increases (decreases) north (south) of the equator (Fig. 2d). This
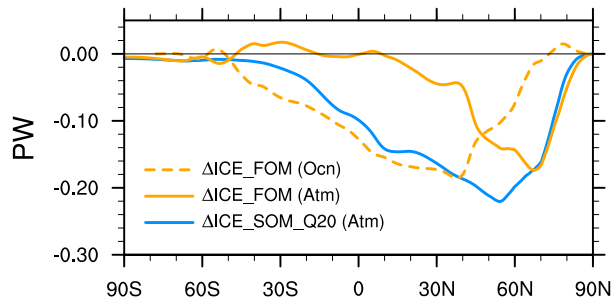
FIG. 3. Annual northward energy transport (PW) response to Arctic sea ice loss in ΔICE_FOM (orange curves: solid for atmosphere, dashed for ocean) and ΔICE_SOM_Q20 (solid blue curve for atmosphere). Note that the ocean heat transport response in ΔICE_SOM_Q20 is identically zero by design.

northward displacement of precipitation in the tropics is consistent with the notion that it is driven by the northward-directed cross-equatorial SST anomaly gradient. Smaller-scale features are evident within this large-scale structure, particularly over the eastern Pacific and Atlantic sectors, indicative of northward shifts in climatological mean precipitation maxima in these locations. In summary, the large-scale tropical precipitation responses to Arctic sea ice loss are nearly orthogonal in the two model configurations and even have opposite sign within the Pacific basin. Another notable distinction is the larger magnitude and broader meridional scale of the tropical precipitation responses in ΔICE_SOM_Q20 compared to ΔICE_FOM.

The SLP responses show similarities and differences between the two models. In ΔICE_SOM_Q20, the most striking feature is the shift of mass out of the NH and into the SH, consistent with the asymmetry in the SST and precipitation responses (Fig. 2f). This asymmetry is less apparent in ΔICE_FOM (Fig. 2e). Both simulations show negative anomalies in the central Arctic and over most of North America, as well as the eastern North Atlantic extending into southern Europe and northern Africa, with larger magnitudes in ΔICE_SOM_Q20 compared to ΔICE_FOM. Zonally oriented high pressure extends over northern Europe across Siberia in both simulations. A notable difference between ΔICE_FOM and ΔICE_SOM_Q20 is the low pressure center response over the North Pacific in the former but not the latter. We diagnose the reason for this difference when we discuss the AMIP simulations below.

In summary, the remote equilibrium surface climate responses to LRF-induced Arctic sea ice loss differ considerably depending upon the physical representation of the ocean. The SST response in the full-depth dynamical ocean shows a large degree of symmetry

about the equator, accompanied by an equatorward intensification of the ITCZs in both hemispheres, whereas the response in the thermodynamic slab-ocean model is mainly antisymmetric about the equator and is associated with a pronounced shift of the ITCZ toward the warmer NH. Next we explore the mechanisms by which the different ocean model configurations alter the surface climate response to Arctic sea ice loss.

b. Northward energy transport response to Arctic sea ice loss

To better understand differences between the remote climate responses in ΔICE_FOM and ΔICE_SOM_Q20, we examine the changes in northward energy transport by the ocean and atmosphere. In ΔICE_FOM, the atmospheric northward energy transport is reduced in the NH extratropics: the atmosphere diverts energy from the high latitudes poleward of 70°N and deposits it at midlatitudes, primarily between 40° and 70°N with a smaller amount going into the tropics (Fig. 3; see also Fig. 10 in D15). This can be understood as a consequence of the fact that Arctic sea ice loss represents an anomalous energy source into the atmosphere, reducing the need for poleward energy transport within the atmosphere under steady-state conditions. The oceanic northward energy transport also diminishes in response to Arctic sea ice loss, with peak amplitude comparable to that in the atmosphere (−0.19 vs −0.17 PW; Fig. 3). However, the oceanic northward energy transport response extends over a broader range of latitudes than the atmospheric response: the ocean transports heat out of the high latitudes (north of 55°N) and deposits that heat relatively uniformly between 40°N and 50°S. The reduction in OHT in response to Arctic sea ice loss is associated with a weakening of the AMOC (not shown). By design, ocean heat transport in ΔICE_SOM_Q20 cannot change; thus, the atmosphere must accomplish the required reduction in northward heat transport in response to Arctic sea ice loss. Indeed, the atmosphere in ΔICE_SOM_Q20 redirects the excess heat vented from the Arctic into the northern midlatitudes and throughout the tropics (Fig. 3).

These results show that differences in the equilibrium global climate response to LRF-induced Arctic sea ice loss in the dynamical and slab-ocean coupled model configurations are attributable to differences in how they respond to the anomalous energy input associated with Arctic sea ice loss, subject to global energy balance constraints. In ΔICE_FOM the ocean and atmosphere more or less split the task of redistributing the excess heat farther south (including into the tropics), whereas
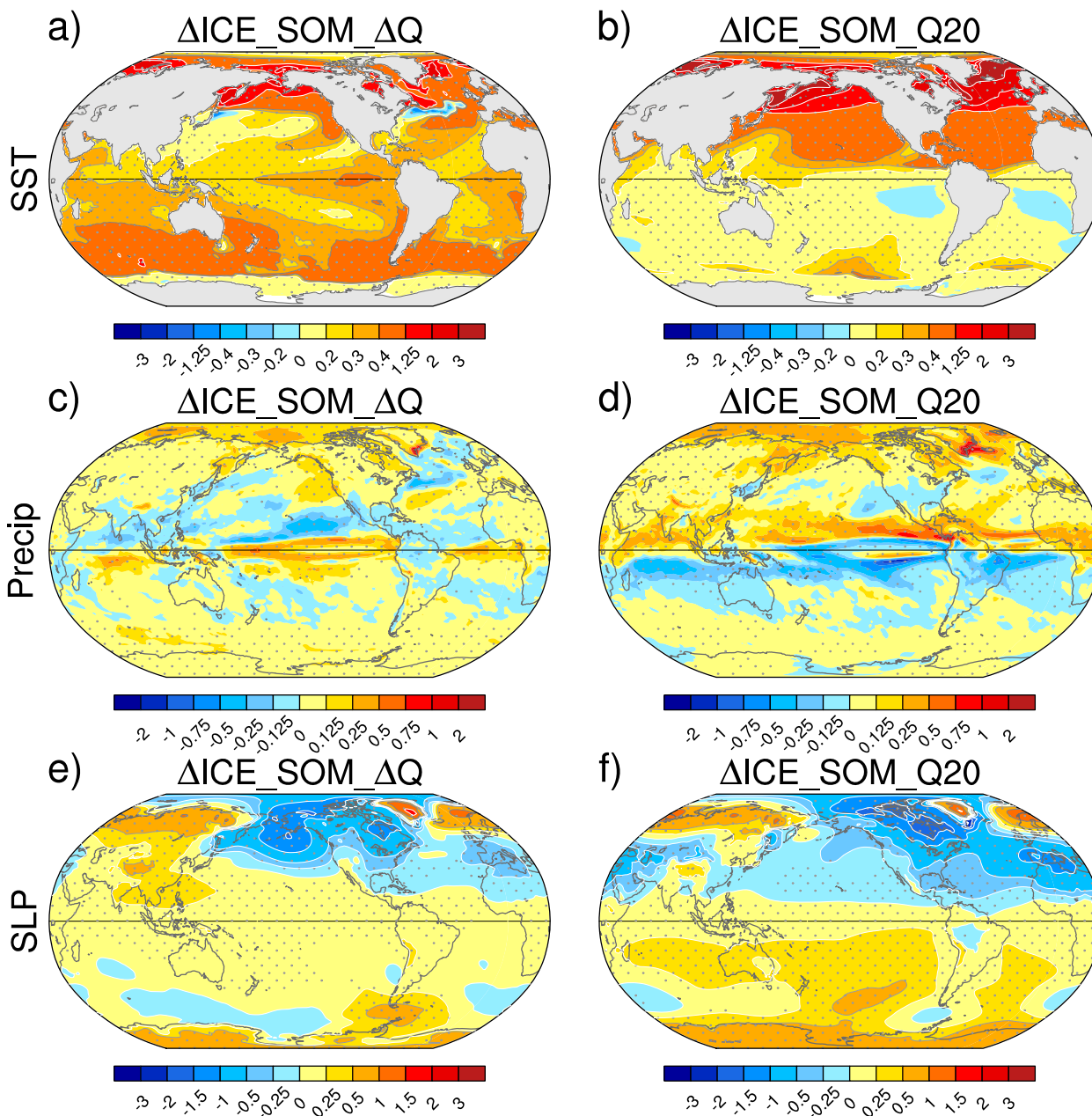
FIG. 4. As in Fig. 2, but for (left) ΔICE_SOM_ΔQ.

in ΔICE_SOM_Q20, the atmosphere necessarily does all the work (see also D15).

c. Impact of ocean heat transport response to Arctic sea ice loss

We hypothesize that oceanic heat transport response to Arctic sea ice loss is responsible for the different surface climate responses in ΔICE_FOM and ΔICE_SOM_Q20. To test this hypothesis, we performed an additional SOM simulation in which ocean heat transport

from ICE21_FOM is specified via a Qflux term. This additional SOM simulation, ICE21_SOM_Q21, upon subtracting ICE20_SOM_Q20, explicitly assesses the contributions of thermodynamic air–sea interaction and changes in oceanic heat transport in the climate response to Arctic sea ice loss in a consistent coupled slab-ocean model framework (recall section 2d). Figure 4 shows global maps of the annual-mean SST, precipitation, and SLP responses in ΔICE_SOM_ΔQ (obtained by subtracting ICE20_SOM_Q20 from ICE21_SOM_Q21); the
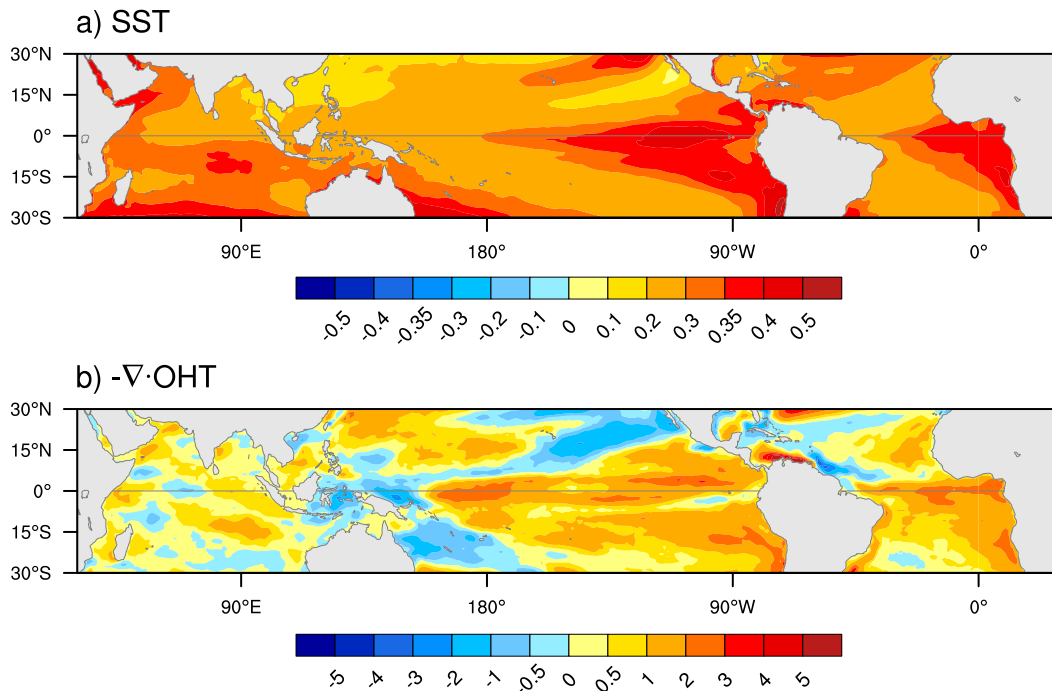
a) SST

b) -∇·OHT

FIG. 5. Annual tropical (a) SST (°C) and (b) ocean heat transport convergence (W m^{-2}) responses in ΔICE_SOM_ΔQ.

corresponding maps based on ΔICE_SOM_Q20 are also shown for reference. The responses are largely similar between ΔICE_SOM_ΔQ and ΔICE_FOM (recall Fig. 2), although the magnitudes are somewhat larger in the former compared to the latter, especially for SST and tropical precipitation. We speculate that the warm bias in ΔICE_SOM_ΔQ is due to some of the heat in ΔICE_FOM still sequestered in the deep ocean and not available to warm the surface. The warm bias notwithstanding, the close agreement between the global structures of the climate responses in ΔICE_SOM_ΔQ and ΔICE_FOM clearly and explicitly implicates ocean heat transport as the reason for the different climate responses to Arctic sea ice loss in the full ocean and slab-ocean coupled model configurations (Fig. 3). In other words, Arctic sea ice loss in these experiments results in an ocean heat transport response that is critically important to the full climate response.

The origin of the equatorial Pacific (and Atlantic) SST response maxima in ΔICE_FOM and ΔICE_SOM_ΔQ is of particular interest because of their potential influence on tropical precipitation that in turn drives global atmospheric teleconnections (see section 3e). The fact that this aspect of the SST response is present in ΔICE_SOM_ΔQ but not in ΔICE_SOM_Q20 implicates ocean dynamics as being important. Figure 5 shows the tropical SST and ocean heat flux convergence responses in ΔICE_SOM_ΔQ (note that the latter is identical to that in ΔICE_FOM). The SST

response maxima in the eastern tropical Pacific and Atlantic are generally associated with anomalous ocean heat transport convergence; that is, ocean dynamics contribute to the SST response maxima in these locations. Other regions (e.g., the far-western Pacific and the northeastern subtropical Pacific) show anomalous ocean heat transport divergence in regions of negative SST response, implying that the SST anomalies in these regions are damped rather than driven by ocean dynamics.

A complete investigation of the processes responsible for the anomalous ocean heat transport convergence in the tropical Pacific in ΔICE_FOM is beyond the scope of this study. However, preliminary analysis suggests that a weakening of the wind-driven oceanic subtropical cells may play a role. Figure 6a shows the tropical surface wind and SST responses to Arctic sea ice loss in ΔICE_FOM. Over the Pacific sector the responses are reminiscent of El Niño, with enhanced warming in the eastern equatorial Pacific accompanied by anomalous westerly winds in the central equatorial Pacific and anomalous wind convergence into the region of maximum SST warming. The westerly wind anomalies reduce the zonal tilt of the equatorial Pacific thermocline, evidenced by the negative (positive) temperature anomalies within the main thermocline in the west (east; Fig. 6b). The anomalous westerlies also weaken the upwelling along the equator and generally reduce the strength of the
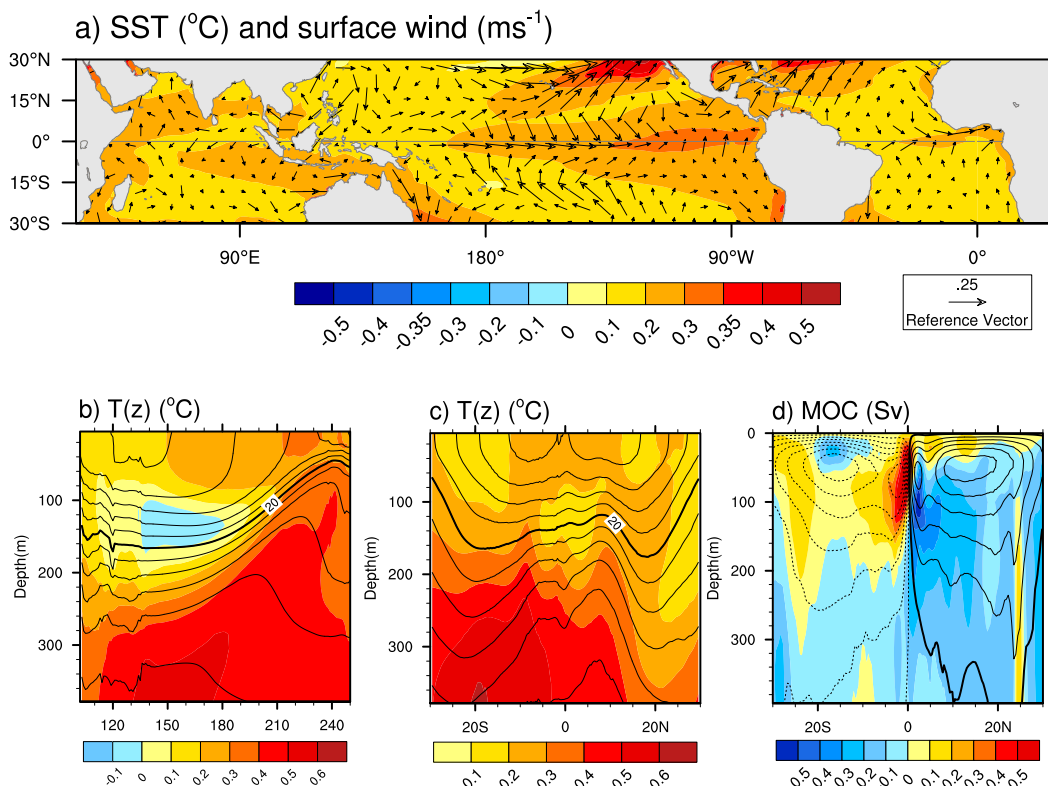
FIG. 6. Annual responses in ΔICE_FOM. (a) Tropical SST (°C) and surface wind vectors, and Pacific Ocean cross sections for (b) temperature (°C) as a function of longitude (°E) and depth along the equator, (c) temperature (°C) as a function of latitude and depth zonally averaged across the Pacific, and (d) meridional overturning circulation (MOC; Sv) as a function of latitude and depth zonally averaged across the Pacific. In (b)–(d), contours show the control (late twentieth century) climatology from ICE20_FOM and shading denotes the response from ΔICE_FOM. Contour intervals for climatologies are 2°C with the 20°C contour thickened in (b),(c) and 5 Sv with the zero contour thickened in (d).

subtropical meridional overturning circulation cells (Fig. 6c). Unlike El Niño, however, the largest warming occurs beneath the main thermocline (below 300 m) in the western equatorial Pacific (Fig. 6b) and south of the equator (Fig. 6d). The mechanisms responsible for the enhanced warming at depth remain to be understood. In summary, it appears that the dynamically induced SST warming maximum in the eastern equatorial Pacific in response to Arctic sea ice loss results from a combination of processes, including diminished equatorial upwelling, weakened stratification, and a general reduction in the strength of the subtropical cells.

We now turn our attention to isolating the component of the climate response that is driven solely by the ocean heat transport response to Arctic sea ice loss. This is accomplished by subtracting ICE21_SOM_Q20 from ICE21_SOM_Q21 to obtain ICE21_SOM_ΔQ (note that this subtraction removes the direct influence of the ice loss since the sea ice conditions in the two experiments are the same). The SST, precipitation, and SLP responses in ICE21_SOM_ΔQ are shown in Fig. 7. Note that these response patterns are shaped by thermodynamic air–sea interaction, although they originate from dynamical ocean changes. The SST response shows, not surprisingly, that ocean heat transport changes in response to Arctic sea ice loss act to cool the NH and warm the SH (Fig. 7a). The NH cooling is strongest in the midlatitudes and in the vicinity of the western boundary currents and their extensions, while the SH warming is most pronounced in the vicinity of the Antarctic Circumpolar Current and the eastern tropical ocean basins. The low-latitude warming maxima south of the equator are consistent with positive thermodynamic feedbacks among higher SSTs, weakened surface winds, and reduced low-level cloudiness (not shown), similar to that described in Xie et al. (2010) for the response to global warming. The precipitation response shows large-scale drying in the NH and moistening in the SH, with the largest changes occurring in the deep tropics (Fig. 7b).
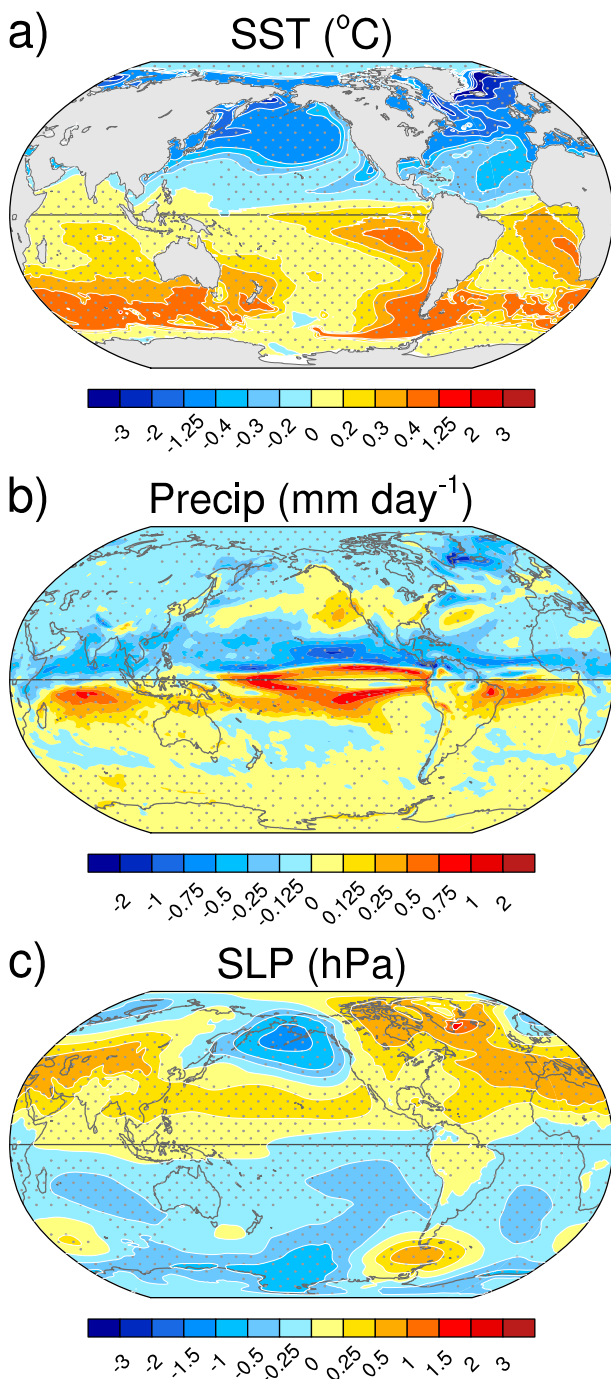
FIG. 7. As in Fig. 2, but for ICE21_SOM_ΔQ.

Finally, the SLP response shows a large-scale pattern of generally positive (negative) anomalies north (south) of the equator, indicative of an overall shift in mass from the SH to the NH (Fig. 7c). This large-scale response is interrupted at high latitudes by a deepening of the Aleutian low in the North Pacific and by a wave train response over the Southern Ocean. As we show next, these features owe

their origin to the precipitation anomalies within the tropics. In general, the climate responses resulting directly from the ocean heat transport response to Arctic sea ice loss are qualitatively similar to those resulting from a weakened Atlantic meridional overturning circulation (AMOC), as obtained by Zhang and Delworth (2005, their Fig. 1d) in sustained freshwater hosing experiments with the GFDL Climate Model, version 2 (CM2.0). The fact that the AMOC weakens by approximately 2 Sv ($1 \, \text{Sv} \equiv 10^6 \, \text{m}^3 \, \text{s}^{-1}$) in ΔICE_FOM (not shown) supports our interpretation. We note also that the deepened Aleutian low response to a weakened AMOC is a robust feature across climate models (Okumura et al. 2009).

d. Additional atmospheric impacts of the oceanic heat transport response to Arctic sea ice loss

In this section, we use the SOM experiments as a test bed for elucidating additional atmospheric impacts of the oceanic heat transport response to Arctic sea ice loss, placing these within the context of the full atmospheric response to Arctic sea ice loss. In particular, we consider aspects of the zonal-mean hydrological cycle, circulation, and temperature responses as a function of height and latitude. Figure 8 shows the atmospheric condensational heating and precipitation responses. In the full response to Arctic sea ice loss (ΔICE_SOM_ΔQ), atmospheric condensational heating shows a global-scale pattern of increase in the upper troposphere and decrease in the lower troposphere, indicative of an upward and poleward shift of the climatological heating maxima in both hemispheres (Fig. 8a). This pattern is similar to that in ΔICE_FOM (not shown, but see Fig. 7a in D15), except for a stronger negative heating response in the upper troposphere of the northern subtropics in the slab-ocean configuration; the reasons for this difference are unclear. Within the tropics, heating in the upper troposphere is enhanced near 5°S and 5°N, slightly equatorward of the climatological mean ITCZ heating maxima. In the Arctic, there is enhanced condensational heating in the boundary layer, consistent with the increase in precipitation. Compared to the high degree of equatorial symmetry in ΔICE_SOM_ΔQ, the condensational heating response in ΔICE_SOM_Q20 is largely antisymmetric about the equator, consistent with the differences in their SST responses (Fig. 8b). In particular, the thermodynamic-only slab-ocean response shows a broad increase in tropospheric heating across most of the NH and a decrease south of the equator mainly in the tropics. Thus, the meridional structures of the tropical heating responses in the two model configurations are nearly
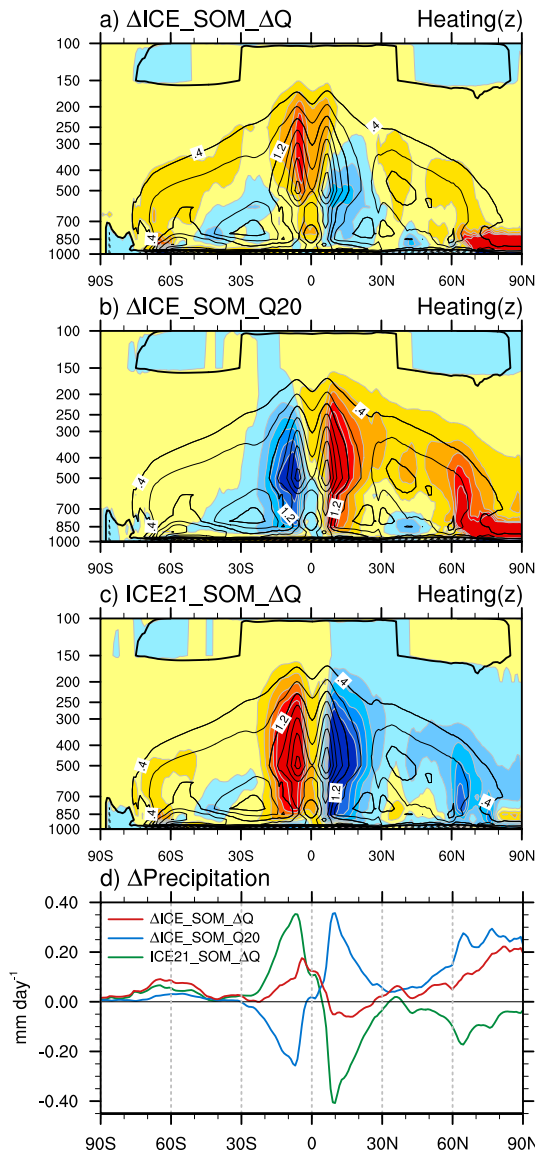
FIG. 8. Annual zonal-mean atmospheric condensational heating rate (K day^{-1}) as a function of latitude and pressure in (a) ΔICE_SOM_ΔQ, (b) ΔICE_SOM_Q20, and (c) ICE21_SOM_ΔQ. Contours show the control (late twentieth century) climatology and shading denotes the response. The contour interval is 0.4 K day^{-1}. (d) Annual zonal-mean precipitation response (mm day^{-1}) in ΔICE_SOM_ΔQ (red), ΔICE_SOM_Q20 (blue), and ICE21_SOM_ΔQ (green).

FIG. 9. Annual zonal-mean atmospheric meridional stream-function (10^{-9} kg s^{-1}) as a function of latitude and pressure (hPa) in (a) ΔICE_SOM_ΔQ, (b) ΔICE_SOM_Q20, and (c) ICE21_SOM_ΔQ. Contours show the control (late twentieth century) climatology and shading denotes the response. Note the different color bar scale in (a) compared to (b),(c). Contour interval for climatology is 2×10^{-8} kg s^{-1}, zero contour is thickened.

orthogonal: the full response shows a narrow equatorward intensification of the ITCZs, while the thermodynamic response shows a broad north–south dipole with increased (decreased) heating on the poleward flank of the northern (southern) branch of the ITCZ indicative of a northward shift of the entire tropical heating maximum. Similar asymmetries are evident in the precipitation responses (Fig. 8d). In addition, the
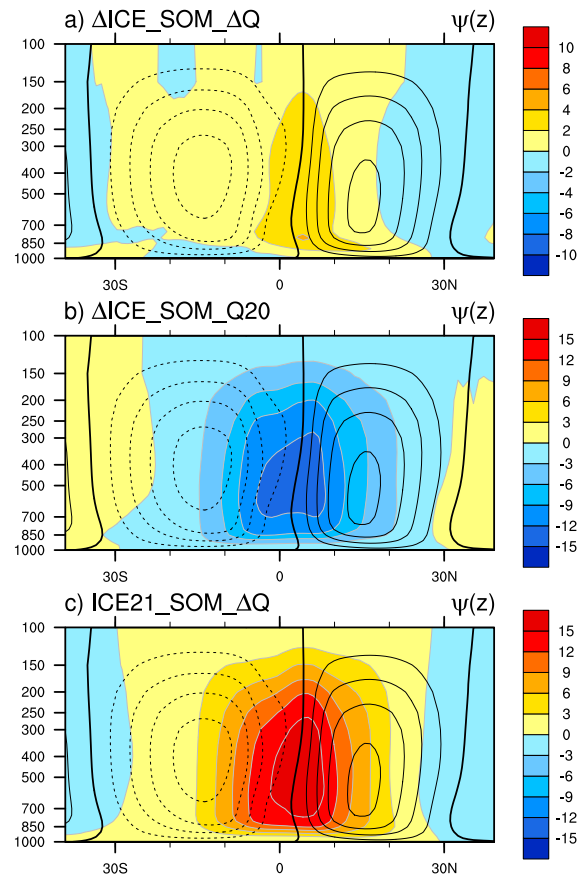
magnitudes of the tropical heating and precipitation responses are considerably larger in ΔICE_SOM_Q20 than in ΔICE_SOM_ΔQ. The role of the ocean heat transport response, identified from ICE21_SOM_ΔQ, is to produce a southward shift of the entire tropical heating maximum that nearly cancels the northward shift as a result of thermodynamic processes (Fig. 8c). A similar compensation is evident in the tropical precipitation responses (Fig. 8d).

The opposing roles of ocean thermodynamics and dynamics in the equilibrium tropical response to LRF-induced Arctic sea ice loss are also evident in the atmospheric meridional streamfunction fields shown in Fig. 9. The thermally direct tropical overturning circulation responses extend from approximately 15°S to 20°N, with

negative values in the case of ΔICE_SOM_Q20 and positive values in the case of ICE21_SOM_ΔQ (Figs. 9b and 9c, respectively). By comparison, the anomalous tropical overturning circulation cell in the full response to Arctic sea ice loss is weakly positive and occupies a narrower latitudinal span (from approximately 2°S to 10°N; Fig. 9a).

Differences in the tropical condensational heating, precipitation, and associated thermally direct overturning circulation cell responses reflect the different mechanisms that transport energy southward in response to Arctic sea ice loss, with and without ocean heat transport changes. If the ocean circulation is allowed to change as in ΔICE_SOM_ΔQ, transporting about half of the total energy southward, the remote climate response exhibits a large degree of symmetry between the NH and SH: the ITCZs increase slightly in strength, owing to a warmer and moisture tropical atmosphere, and shift slightly equatorward in response to the local equatorial SST warming maximum. On the other hand, in the absence of an ocean heat transport response as in ΔICE_SOM_Q20, there is a shift of the entire Hadley circulation into the NH in response to stronger warming in the NH compared to the SH. This shift of the Hadley circulation is the mechanism whereby anomalous energy is transported by the atmosphere across the equator (e.g., Kang et al. 2008; Hwang and Frierson 2010).

The corresponding zonal-mean atmospheric temperature and zonal wind responses are shown in Fig. 10. Both ΔICE_SOM_ΔQ and ΔICE_SOM_Q20 show similar patterns of response in the northern extratropics, although the magnitudes are approximately 15%–20% smaller in the former because the ocean has transported some of the energy out of the Arctic. The thermal response shows surface-intensified warming in the Arctic that extends through the depth of the troposphere, with cooling in the lower stratosphere (Figs. 10a,c). Thermal wind balance dictates that easterly wind anomalies occur on the equatorward side of the anomalous meridional temperature gradient (in the latitude band 50°–70°N), peaking in strength in the mid-to-upper troposphere (maximum values ~1 m s^{-1}; Figs. 10b,d). These easterly anomalies represent an equatorward contraction of the mean westerly jet in response to Arctic sea ice loss. In addition to an equatorward contraction, the westerly jet in ΔICE_SOM_ΔQ shifts southward because of the presence of westerly wind anomalies in the latitude band 20°–40°N. The remote responses are quite distinct in the two experiments, with ΔICE_SOM_ΔQ characterized by strong symmetry about the equator and ΔICE_SOM_Q20

showing a large asymmetric component, particularly in the temperature field and consistent with earlier discussion.

The temperature and zonal wind responses to the ocean heat transport change in isolation is shown in the lower panels of Fig. 10. The thermal response shows cooling of the NH extratropical troposphere and warming of the entire SH troposphere and northern tropics (Fig. 10e). Within the tropics, the warming is largest in the upper troposphere. The cooling in the NH is greater than the warming to the south, presumably reflecting changes in the TOA energy balance and horizontal transport by the atmosphere. Upper-tropospheric and lower-stratospheric westerlies in the NH and upper-tropospheric easterlies in the SH dominate the zonal wind response (Fig. 10f). Both of these features are located on the equatorward side of climatological mean jets. The westerly anomalies in the NH are stronger than the easterly anomalies in the SH, consistent with differences in the strength of the extratropical temperature responses.

e. Tropical impact on extratropical circulation response to Arctic sea ice loss

A conspicuous difference between the SLP responses in ΔICE_SOM_ΔQ and ΔICE_SOM_Q20 is the presence of a low pressure center over the North Pacific in the former but not the latter (recall Figs. 4e,f). Previous studies have implicated tropical SST anomalies and associated changes in precipitation and latent heat release as a driver of midlatitude circulation anomalies via Rossby wave dynamics, particularly during the winter season (e.g., Horel and Wallace 1981; Trenberth et al. 1998; Ding et al. 2014). We now ask, Do tropical SST changes (driven by the ocean heat transport response to Arctic sea ice loss) result in atmospheric teleconnections that propagate back into the midlatitudes? To address this question, we use the AMIP simulations described in section 2e.

Figure 11 compares the boreal winter [December–February (DJF)] precipitation and SLP responses in ICE21_SOM_ΔQ (Figs. 11a,d) with those in the global (ICE21_AMIPG_ΔQ; Figs. 11b,e) and tropical (ICE21_AMIPT_ΔQ; Figs. 11c,f) AMIP simulations. The high degree of resemblance between the responses in ICE21_SOM_ΔQ (Figs. 11a,d) and ICE21_AMIPG_ΔQ (Figs. 11b,e) validates the utility of the AMIP approach. Further, comparison between ICE21_AMIPG_ΔQ and ICE21_AMIPT_ΔQ (Figs. 11c,f) demonstrates that tropical SST changes are responsible for much of the midlatitude circulation response in ICE21_AMIPG_ΔQ and by extension ICE21_SOM_ΔQ, including the
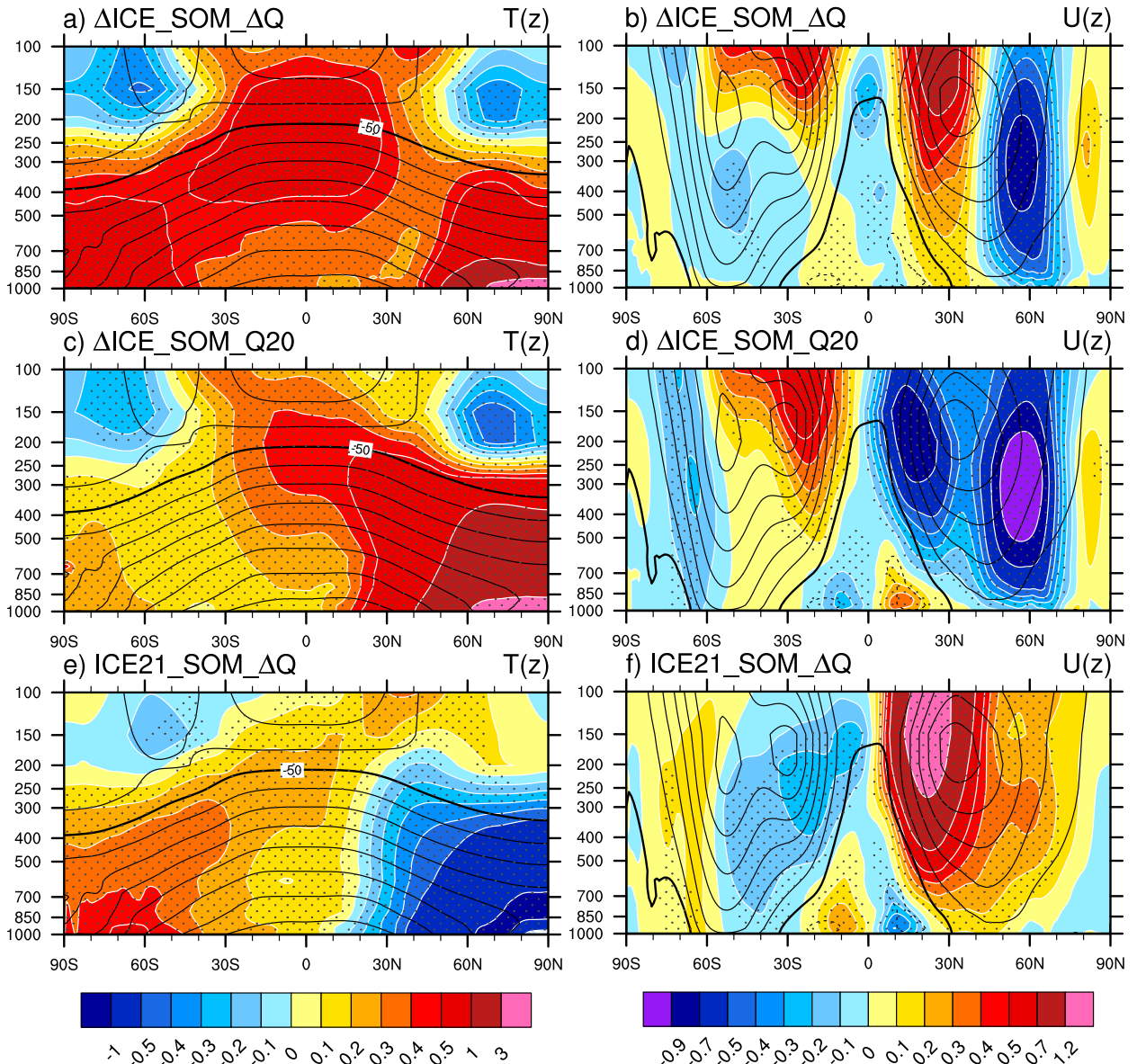
FIG. 10. Annual zonal-mean (left) air temperature (°C) and (right) zonal wind (m s^{-1}) responses to Arctic sea ice loss as a function of latitude and pressure in (a),(b) ΔICE_SOM_ΔQ, (c),(d) ΔICE_SOM_Q20, and (e),(f) ICE21_SOM_ΔQ. Contours show the control (late twentieth century) climatology and shading denotes the response. Contour interval for climatology is 10°C for air temperature and 5 m s^{-1} for zonal wind. The −50°C isotherm for temperature and zero contour for zonal wind are thickened.

deepened Aleutian low over the North Pacific and the east–west SLP dipole across the Southern Ocean, as well as part of the high pressure response over the North Atlantic; however, the SLP response over eastern Eurasia is not attributable to tropical SST changes. This result confirms the key role of tropical SST anomalies induced by anomalous ocean heat transport convergence for both the tropical and midlatitude atmospheric circulation responses to Arctic sea ice loss. Similar results are found for the annual mean responses,

which resemble those in DJF but with weaker amplitude (not shown).

4. Discussion

a. Extratropical forcing of tropical teleconnections

The most fundamental outcome of this study relates to the vastly differing global-scale equilibrium climate responses to LRF-induced Arctic sea ice loss
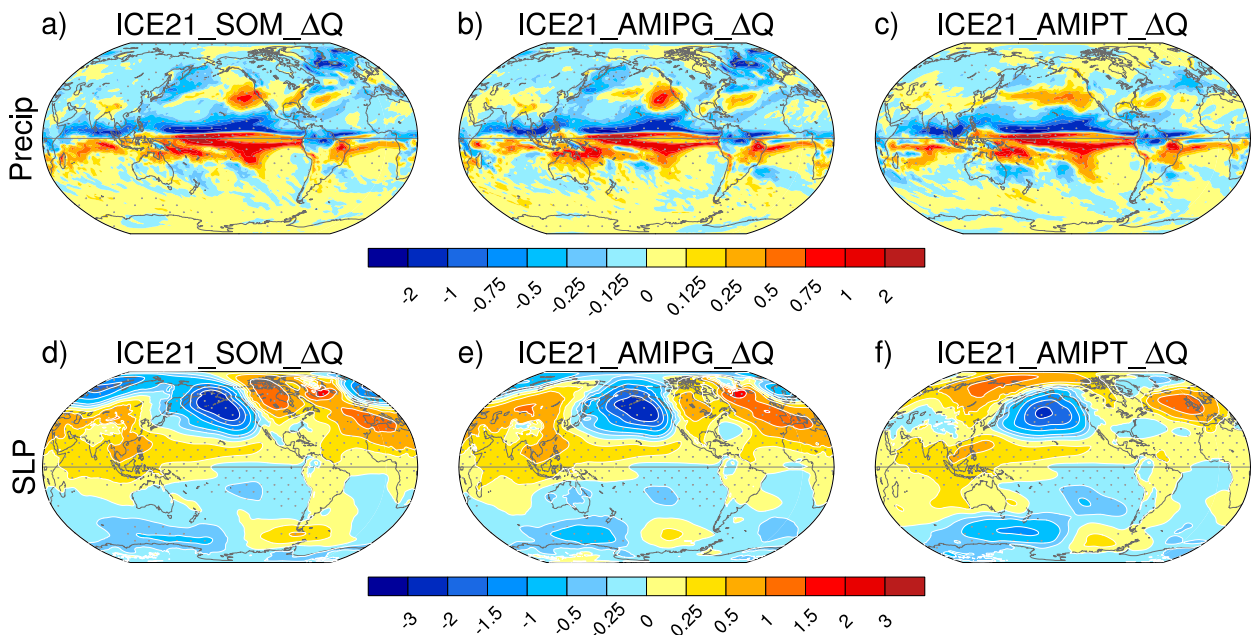
FIG. 11. December–February (a)–(c) precipitation (mm day^{-1}) and (d)–(f) SLP (hPa) responses in (left) ICE21_SOM_ΔQ, (center) ICE21_AMIPG_ΔQ, and (right) ICE21_AMIPT_ΔQ.

obtained with a slab versus dynamical ocean coupled model. In particular, the response is largely symmetric about the equator in the dynamic ocean configuration and mainly antisymmetric in the thermodynamic slab-ocean setting. This difference in global structure stems from a reduction in northward OHT and associated increase in OHT convergence in the tropics in the dynamical ocean model, a process absent in the slab-ocean simulation. The resulting dynamically induced warming of the tropical SSTs, with a local maximum along the equator particularly in the Pacific, leads to an equatorward intensification of the ITCZs. In contrast, the slab-ocean setting produces a pronounced interhemispheric SST gradient that in turn displaces the ITCZ northward toward the warmed NH. The tropical atmospheric circulation responses are also distinctive in the two ocean model configurations, with a strong and broad northward shift of the Hadley circulation in the slab-ocean configuration compared to a weak and equatorially confined atmospheric response in the dynamical ocean setting.

The latitudinal shift of the ITCZ in response to Arctic sea ice loss in our slab-ocean coupled model experiment (ΔICE_SOM_Q20) is analogous to that found in response to North Atlantic cooling (Cvijanovic and Chiang 2013) and sea ice expansion during the Last Glacial Maximum (Chiang and Bitz 2005; Broccoli et al. 2006) based on slab-ocean coupled models. In a broader context, this thermodynamic response is a manifestation of a global interhemispheric

teleconnection hypothesized by Chiang and Friedman (2012). They argue that the ITCZ response is driven by thermal contrasts between the hemispheres and the need to transport energy out of (into) the heated (cooled) hemisphere. Similar energetic constraints are invoked by Kang et al. (2008) and Frierson and Hwang (2012) for understanding the climate response to idealized extratropical thermal forcings in a slab-ocean setting, although Cvijanovic and Chiang (2013) emphasize the importance of tropical SST changes for the ITCZ response. Here, we find that if ocean dynamics are allowed to respond to the imposed thermal perturbation (in our case Arctic sea ice loss), the resulting change in northward ocean OHT mitigates the need for a strong equilibrium tropical atmospheric response (e.g., ITCZ shift). Similar results were obtained by Kay et al. (2015) using a very different type of thermal perturbation—namely, a decrease in cloud liquid water content over the Southern Ocean. It remains to be seen whether thermal forcings at other latitudes elicit similar responses to those found here and in Kay et al. (2015) and how sensitive these responses are to the particular dynamical ocean model employed.

We emphasize that our results confirm the importance of northward OHT in controlling the latitudinal position of the ITCZ and Hadley circulation, in keeping with the mechanisms reviewed in Schneider et al. (2014). The distinction made here is to show that when both the oceanic and atmospheric northward

heat transports are free to respond to Arctic sea ice loss, their combined influence on the climate system differs from that of either one in isolation. Specifically, the thermodynamic and dynamic components of the coupled response to Arctic sea ice loss both exhibit strong hemispheric asymmetries, but these largely cancel, leaving a net response that is approximately symmetric about the equator. A full understanding of this result within an energetics framework remains for future work.

b. Origin of the tropical SST response

The increase in tropical SSTs in response to Arctic sea ice loss, although small in magnitude, is critically important because of its influence on the atmospheric circulation both in the tropics and midlatitudes. This tropical SST warming results from an increase in OHT convergence (e.g., air–sea fluxes would act to cool the SSTs). Further work is needed to understand the mechanisms responsible for the increased tropical OHT convergence, although preliminary results suggest that a combination of processes contribute, including ENSO-like dynamics, wind-driven changes in the subtropical overturning cells, and warming beneath the main thermocline. It is interesting to note that the pattern of tropical SST anomalies induced by the dynamical ocean response to Arctic sea ice loss shows enhanced warming in the southeastern portion of each basin, with largest amplitudes in the Pacific. This pattern resembles that of the southern "meridional modes," intrinsic structures of SST variability resulting from thermodynamic air–sea interaction (Zhang et al. 2014). This resemblance is particularly striking after the zonal-mean SST response to Arctic sea ice loss is removed (not shown). As discussed in Chang et al. (2007) and Zhang et al. (2014), the South Pacific meridional mode can act as a trigger for ENSO, a coupled ocean–atmosphere phenomenon in which equatorial ocean dynamics and dynamical air–sea feedbacks play a key role (e.g., Neelin 2011). We conjecture that a similar mechanism may be at work in the fully coupled model response to Arctic sea ice loss, potentially explaining the eastern equatorial Pacific SST warming maximum. Further experiments are needed to evaluate this idea.

c. Midlatitude circulation changes forced by Arctic sea ice loss via the tropics

A notable finding from this study is that Arctic sea ice loss alters tropical SSTs and precipitation, which in turn force atmospheric teleconnections back into midlatitudes. This highlights both the global nature and complexity of possible pathways for the equilibrium climate response to Arctic sea ice loss when both thermodynamic and dynamic air–sea interactions are included. It also demonstrates the added utility of using a fully coupled model in place of an atmosphere-only or atmosphere–slab ocean model to investigate the response to Arctic sea ice loss. The role of the tropics as a conduit for high-latitude perturbations has also been demonstrated in the North Atlantic "freshwater hosing" and "cooling" experiments of Okumura et al. (2009) and Cvijanovic and Chiang (2013), respectively.

5. Summary

We investigated the role of ocean dynamics, in particular ocean heat transport, in the equilibrium coupled climate response to projected Arctic sea ice loss in the CCSM4 at 1° latitude–longitude spatial resolution. To isolate the role of the ocean dynamical response, we conducted coupled model experiments using a slab-ocean configuration, with and without the changes in ocean heat transport that occur in response to ice loss in CCSM4. Additional atmosphere-only simulations using SSTs from the slab-ocean experiments provided further insight into the role of tropical and extratropical SST responses for the global atmospheric circulation response.

Without including the effects of ocean heat transport response, the remote atmospheric response is hemispherically asymmetric, with strong warming extending from the Arctic and decreasing monotonically toward the equator and little warming in the SH. This pattern is associated with a broad northward shift of the tropical precipitation distribution and Hadley circulation and a global-scale displacement atmospheric mass from the hemisphere with the ice loss and into the other hemisphere. The ITCZ and/or Hadley cell shift is consistent with that noted in previous works investigating the atmospheric response to altered sea ice conditions and other more idealized extratropical thermal forcings (Chiang and Bitz 2005; Kang et al. 2008; Chiang and Friedman 2012; Seo et al. 2014; Schneider et al. 2014). With the ocean heat transport response, the remote atmospheric response becomes more symmetric about the equator, with comparable warming in both hemispheres and a weak equatorward intensification of the Pacific ITCZs. The symmetric equatorward intensification of the ITCZs is associated with enhanced SST warming along the equator in the eastern Pacific driven by anomalous ocean heat transport convergence. This dynamically induced tropical Pacific SST–precipitation response drives atmospheric circulation

teleconnections that propagate as Rossby waves to the northern and southern midlatitudes.

Our results highlight the global interconnectivity inherent in the coupled climate system, whereby Arctic sea ice loss induces a remote response in the tropics via ocean heat transport changes, and the tropical SST–precipitation response in turn drives atmospheric circulation changes in the extratropics via Rossby wave dynamics. It remains to be seen how sensitive these findings are to the particular climate model employed and whether other types of extratropical forcings elicit similar dynamic and thermodynamic ocean feedbacks. However, our results suggest that studies based on slab-ocean models may potentially misconstrue the true nature of the equilibrium global climate response to a given forcing, including those relevant for paleoclimate applications. Additional experiments will be required to determine if this is the case. Future work will examine transient adjustment of the global coupled climate system to Arctic sea ice loss, with a particular focus on the time scales and mechanisms of the dynamical ocean response.

REFERENCES

Barnes, E. A., 2013: Revisiting the evidence linking arctic amplification to extreme weather in midlatitudes. *Geophys. Res. Lett.*, **40**, 4728–4733, doi:10.1002/grl.50880.

——, and J. A. Screen, 2015: The impact of arctic warming on the midlatitude jetstream: Can it? Has it? Will it? *Wiley Interdiscip. Rev.: Climate Change*, **6**, 277–286, doi:10.1002/wcc.337.

Bitz, C. M., K. M. Shell, P. R. Gent, D. A. Bailey, G. Danabasoglu, K. C. Armour, M. M. Holland, and J. T. Kiehl, 2012: Climate sensitivity of the Community Climate System Model version 4. *J. Climate*, **25**, 3053–3070, doi:10.1175/JCLI-D-11-00290.1.

Broccoli, A. J., K. A. Dahl, and R. J. Stouffer, 2006: Response of the ITCZ to Northern Hemisphere cooling. *Geophys. Res. Lett.*, **33**, L01702, doi:10.1029/2005GL024546.

Chang, P., L. Zhang, R. Saravanan, D. J. Vimont, J. C. H. Chiang, L. Ji, H. Seidel, and M. K. Tippett, 2007: Pacific meridional mode and El Nino–Southern Oscillation. *Geophys. Res. Lett.*, **34**, L16608, doi:10.1029/2007GL030302.

Chiang, J. C. H., and C. M. Bitz, 2005: Influence of high latitude ice on the marine intertropical convergence zone. *Climate Dyn.*, **25**, 477–496, doi:10.1007/s00382-005-0040-5.

——, and A. R. Friedman, 2012: Extratropical cooling, interhemispheric thermal gradients, and tropical climate change. *Annu. Rev. Earth Planet. Sci.*, **40**, 383–412, doi:10.1146/annurev-earth-042711-105545.

Cohen, J., and Coauthors, 2014: Recent arctic amplification and extreme mid-latitude weather. *Nat. Geosci.*, **7**, 627–637, doi:10.1038/ngeo2234.

Cvijanovic, I., and J. C. H. Chiang, 2013: Global energy budget changes to high latitude North Atlantic cooling and the tropical ITCZ response. *Climate Dyn.*, **40**, 1435–1452, doi:10.1007/s00382-012-1482-1.

Deser, C., R. Tomas, M. Alexander, and D. Lawrence, 2010: The seasonal atmospheric response to projected arctic sea ice loss in the late twenty-first century. *J. Climate*, **23**, 333–351, doi:10.1175/2009JCLI3053.1.

——, ——, and L. Sun, 2015: The role of ocean–atmosphere coupling in the zonal-mean atmospheric response to arctic sea ice loss. *J. Climate*, **28**, 2168–2186, doi:10.1175/JCLI-D-14-00325.1.

Ding, Q., J. M. Wallace, D. S. Battisti, E. J. Steig, A. J. E. Gallant, H. J. Kim, and L. Geng, 2014: Tropical forcing of the recent rapid arctic warming in northeastern Canada and Greenland. *Nature*, **509**, 209–212, doi:10.1038/nature13260.

Frierson, D. M. W., and Y.-T. Hwang, 2012: Extratropical influence on ITCZ shifts in slab ocean simulations of global warming. *J. Climate*, **25**, 720–733, doi:10.1175/JCLI-D-11-00116.1.

Gent, P., and Coauthors, 2011: The Community Climate System Model version 4. *J. Climate*, **24**, 4973–4991, doi:10.1175/2011JCLI4083.1.

Harvey, B. J., L. C. Shaffrey, and T. J. Woollings, 2014: Equator-to-pole temperature differences and the extra-tropical storm track responses of the CMIP5 climate models. *Climate Dyn.*, **43**, 1171–1182, doi:10.1007/s00382-013-1883-9.

——, ——, and ——, 2015: Deconstructing the climate change response of the Northern Hemisphere wintertime stormtracks. *Climate Dyn.*, **45**, 2847–2860, doi:10.1007/s00382-015-2510-8.

Holland, M. M., D. A. Bailey, B. P. Briegleb, B. Light, and E. Hunke, 2012: Improved sea ice shortwave radiation physics in CCSM4: The impact of melt ponds and black carbon. *J. Climate*, **25**, 1413–1430, doi:10.1175/JCLI-D-11-00078.1.

Horel, J. D., and J. M. Wallace, 1981: Planetary-scale atmospheric phenomena association with the Southern Oscillation. *Mon. Wea. Rev.*, **109**, 813–829, doi:10.1175/1520-0493(1981)109<0813:PSAPAW>2.0.CO;2.

Hwang, Y.-T., and D. M. W. Frierson, 2010: Increasing atmospheric poleward energy transport with global warming. *Geophys. Res. Lett.*, **37**, L24807, doi:10.1029/2010GL045440.

Kang, S. M., I. M. Held, D. M. W. Frierson, and M. Zhao, 2008: The response of the ITCZ to extratropical thermal forcing: Idealized slab-ocean experiments with a GCM. *J. Climate*, **21**, 3521–3532, doi:10.1175/2007JCLI2146.1.

Kay, J. E., V. Yettella, B. Medeiros, C. Hannay, P. Caldwell, and C. Bitz, 2015: Global climate impacts of fixing the Southern Ocean shortwave radiation bias in the Community Earth System Model (CESM). *J. Climate*, **29**, 4617–4636, doi:10.1175/JCLI-D-15-0358.1.

Lehner, F., A. Born, C. C. Raible, and T. F. Stocker, 2013: Amplified inception of European Little Ice Age by sea ice–ocean–atmosphere feedbacks. *J. Climate*, **26**, 7586–7602, doi:10.1175/JCLI-D-12-00690.1.

Mori, M., M. Watanabe, H. Shiogama, J. Inoue, and M. Kimoto, 2014: Robust arctic sea-ice influence on the frequent Eurasian cold winters in past decades. *Nat. Geosci.*, **7**, 869–873, doi:10.1038/ngeo2277.

Neelin, J. D., 2011: *Climate Change and Climate Modeling*. Cambridge University Press, 282 pp.

Okumura, Y. M., C. Deser, A. Hu, A. Timmermann, and S.-P. Xie, 2009: North Pacific climate response to freshwater forcing in the subarctic North Atlantic: Oceanic and atmospheric pathways. *J. Climate*, **22**, 1424–1445, doi:10.1175/2008JCLI2511.1.

Peings, Y., and G. Magnusdottir, 2014: Response of the wintertime Northern Hemisphere atmospheric circulation to current and projected arctic sea ice decline: A numerical study with CAM5. *J. Climate*, **27**, 244–264, doi:10.1175/JCLI-D-13-00272.1.

Schneider, T., T. Bischoff, and G. H. Haug, 2014: Migrations and dynamics of the intertropical convergence zone. *Nature*, **513**, 45–53, doi:10.1038/nature13636.

Screen, J. A., 2014: Arctic amplification decreases temperature variance in northern mid- to high-latitudes. *Nat. Climate Change*, **4**, 577–582, doi:10.1038/nclimate2268.

——, and I. Simmonds, 2010: Increasing fall–winter energy loss from the Arctic Ocean and its role in arctic temperature amplification. *Geophys. Res. Lett.*, **37**, L16797, doi:10.1029/2010GL044136.

——, and ——, 2013: Exploring links between arctic amplification and mid-latitude weather. *Geophys. Res. Lett.*, **40**, 959–964, doi:10.1002/grl.50174.

——, C. Deser, and L. Sun, 2015a: Reduced risk of North American cold extremes due to continued sea ice loss. *Bull. Amer. Meteor. Soc.*, **96**, 1489–1503, doi:10.1175/BAMS-D-14-00185.1.

——, ——, and ——, 2015b: Projected changes in regional climate extremes arising from arctic sea ice loss. *Environ. Res. Lett.*, **10**, 084006, doi:10.1088/1748-9326/10/8/084006.

Seo, J., S. M. Kang, and D. M. W. Frierson, 2014: Sensitivity of intertropical convergence zone movement to the latitudinal position of thermal forcing. *J. Climate*, **27**, 3035–3042, doi:10.1175/JCLI-D-13-00691.1.

Serreze, M. C., and R. G. Barry, 2011: Processes and impacts of arctic amplification: A research synthesis. *Global Planet. Change*, **77**, 85–96, doi:10.1016/j.gloplacha.2011.03.004.

Sewall, J. O., and L. C. Sloan, 2004: Disappearing arctic sea ice reduces available water in the American west. *Geophys. Res. Lett.*, **31**, L06209, doi:10.1029/2003GL019133.

Sun, L., C. Deser, and R. A. Tomas, 2015: Mechanisms of stratospheric and tropospheric circulation response to projected arctic sea ice loss. *J. Climate*, **28**, 7824–7845, doi:10.1175/JCLI-D-15-0169.1.

Trenberth, K. E., G. W. Branstator, D. Karoly, A. Kumar, N.-C. Lau, and C. Ropelewski, 1998: Progress during TOGA in understanding and modeling global teleconnections associated with tropical sea surface temperatures. *J. Geophys. Res.*, **103**, 14 291–14 324, doi:10.1029/97JC01444.

Xie, S.-P., C. Deser, G. A. Vecchi, J. Ma, H. Teng, A. T. Wittenberg, 2010: Global warming pattern formation: sea surface temperature and rainfall. *J. Climate*, **23**, 966–986, doi:10.1175/2009JCLI3329.1.

Zhang, H., A. Clement, and P. DiNezio, 2014: The South Pacific meridional mode: A mechanism for ENSO-like variability. *J. Climate*, **27**, 769–783, doi:10.1175/JCLI-D-13-00082.1.

Zhang, R., and T. L. Delworth, 2005: Simulated tropical response to a substantial weakening of the Atlantic thermohaline circulation. *J. Climate*, **18**, 1853–1860, doi:10.1175/JCLI3460.1.